Tominaga et al. *EPJ Quantum Technology* (2025) 12:60
https://doi.org/10.1140/epjqt/s40507-025-00367-w

EPJ Quantum Technology
a SpringerOpen Journal

RESEARCH Open Access

Intrinsic quality factors approaching 10 million in superconducting planar resonators enabled by spiral geometry

Yusuke Tominaga[1*], Shotaro Shirai[1,2], Yuji Hishida[3], Hirotaka Terai[3] and Atsushi Noguchi[1,2,4*]

*Correspondence:
yusuke.tominaga@riken.jp;
u-atsushi@g.ecc.u-tokyo.ac.jp
[1]RIKEN Center for Quantum Computing, Wako, 351-0198 Saitama, Japan
Full list of author information is available at the end of the article

Abstract

This study investigates the use of spiral geometry in superconducting resonators to achieve high intrinsic quality factors, crucial for applications in quantum computation and quantum sensing. We fabricated Archimedean Spiral Resonators (ASRs) using domain-matched epitaxially grown titanium nitride (TiN) on silicon wafers, achieving intrinsic quality factors of $Q_i = (9.6 \pm 1.5) \times 10^6$ at the single-photon level and $Q_i = (9.91 \pm 0.39) \times 10^7$ at high power, which is more than twice as high as those for coplanar waveguide (CPW) resonators under identical conditions on the same chip. We conducted a comprehensive numerical analysis using COMSOL to calculate surface participation ratios (PRs) at critical interfaces: metal-air, metal-substrate, and substrate-air. Our findings reveal that ASRs have lower PRs than CPWs, explaining their superior quality factors and reduced coupling to two-level systems (TLSs).

Keywords: Superconducting resonators; Two-level systems; Surface participation ratio

1 Introduction

Superconducting resonators are fundamental components in cutting-edge quantum technologies, playing essential roles in quantum sensing and quantum computation. They function as readout devices for superconducting quantum bits [1, 2], facilitate qubit interconnections [3], serve as quantum limited amplifiers [4], and enable single-photon detection [5]. Additionally, these devices are the key to storing and manipulating quantum information [6] exemplified by bosonic encoding [7, 8]. However, their practical applications face a constraint in the form of the energy decay time, which is quantified by the intrinsic quality factor Q_i of the resonator. A higher Q_i indicates longer coherence times, making its improvement a primary focus in the development of superconducting resonators for quantum technologies.

Three-dimensional cavity resonators, where the energy is stored within the dielectric medium inside the cavity (typically vacuum or a low-loss dielectric), have achieved exceptional Q_i as high as 10^8 [9–11], enabling breakthroughs such as break-even bosonic encoding for quantum error correction [12, 13]. Despite their performance, the large size and complexity of cavity resonators pose challenges for scalability.

In contrast, planar resonators—primarily two-dimensional conductor structures, such as microstrip lines or coplanar waveguides (CPWs)—are more scalable. They are fabricated on a substrate, with their electromagnetic fields concentrated between the resonator conductors, that is, in the gaps of a stripline or coplanar waveguide. The planar structure allows for fabrication using standard semiconductor processes such as photolithography and etching, and these resonators integrate seamlessly with planar superconducting qubits, making coupling straightforward. However, electromagnetic waves leaking into the substrate or surrounding space lead to radiation and dielectric losses, usually resulting in a lower Q_i than cavity resonators. Recent advancements in surface treatment techniques [14–16] and material investigation [17–19] have shown promising results in enhancing the performance of planar resonators, with recent achievements reaching several million in the single-photon regime using epitaxial tantalum thin films [20].

Hybrid designs aim to combine the high Q_i of 3D designs with the scalability of 2D structures [21, 22], where these resonators have essentially planar structures with additional 3D characteristics. For example, planar conductor patterns on a substrate combine with shielding or encapsulating structures to form a quasi-3D electromagnetic field distribution. While these hybrid architectures offer better performance than purely planar designs and maintain some degree of design flexibility, they still fall short in terms of the integration required for large-scale quantum computing systems. As such, the development of high-quality planar resonators remains critical for achieving fault-tolerant quantum computers. Optimization of the electric field distribution has been identified as a key factor in improving the Q_i of resonators.

A major limitation of planar resonators is energy dissipation due to two-level systems (TLSs) at material interfaces, which dominate losses at low temperatures and low power levels. The TLSs, which originate from material defects or disorder in the amorphous interface layer [23, 24] forming tunneling states [25], can absorb energy from the resonator through capacitive coupling [26] and dissipate it to their own environments. TLS-induced losses not only limit qubit lifetimes and gate fidelities but also pose challenges for implementing bosonic codes, which require high-coherence resonators to encode quantum information in continuous-variable states. Consequently, understanding and mitigating TLS effects is crucial for improving planar resonator performance.

In this study, we explore alternative geometries to reduce coupling to TLSs in planar resonators, focusing on the use of Archimedean Spiral Resonators (ASRs). The spiral geometry distributes the electric field more evenly across the structure, reducing field concentration at the lossy interface and thus minimizing TLS-induced dissipation. In addition, compared to CPWs, the high impedance of ASRs facilitates strong capacitive coupling to the qubit. Unlike many complex resonator geometries, ASRs have well-established analytical models describing their resonance frequencies, impedance, and current distributions [27, 28], which allows for precise theoretical predictions and facilitates efficient design optimizations compared to structures requiring full numerical simulations.

To validate the advantage in Q_i, we fabricated ASRs using domain-matched epitaxially grown titanium nitride (TiN) films on silicon wafers. Our measurements demonstrated intrinsic quality factors of $Q_i = (9.6 \pm 1.5) \times 10^6$ at the single-photon level and $Q_i = (9.91 \pm 0.39) \times 10^7$ at high power, which is more than twice as high as those for CPWs under identical conditions on the same chip.

We also conducted a comprehensive numerical analysis of the surface participation ratios (PRs) for both spiral resonators and CPWs using the finite element solver COMSOL [29]. This analysis examined PR contributions from three critical interfaces: metal-air (MA), metal-substrate (MS), and substrate-air (SA), following methodologies widely employed in the study of microwave losses in superconducting materials [9, 30–33]. These calculations provide insight into the electromagnetic field distribution and energy storage mechanisms in these different resonator geometries.

The outline of this paper is as follows. In Sect. 2, we describe the design principles and theoretical foundations of coplanar waveguides and spiral resonators, including their frequency and impedance calculations, and detail our fabrication process and experimental setup. Section 3 presents our measurement results and analysis of the quality factors of the resonators. Finally, Sect. 4 examines the participation ratios to explain the superior performance of spiral geometries.

2 Design and fabrication

CPWs are the widely adopted choice for the design of superconducting planar resonators due to their simplicity and well-understood behavior. The characteristic frequency f_{CPW} and impedance Z_{CPW} of a CPW can be calculated using the parameters $k_1 = w/g$ and $k_2 = \tanh(\pi w/2h)/\tanh(\pi g/2h)$, where w is the center conductor width, g is the sum of the center conductor width plus the gaps on either side, and h is the distance between the upper shielding and CPW. The equations for quarter-wavelength CPWs are as follows [34]:

$$f_{\mathrm{CPW}} = \frac{c}{4l\sqrt{\epsilon_{\mathrm{eff}}}} \tag{1}$$

$$Z_{\mathrm{CPW}} = \frac{60\pi}{\sqrt{\epsilon_{\mathrm{eff}}}} \left(\frac{K(k_1)}{K(k_1')} + \frac{K(k_2)}{K(k_2')} \right)^{-1}, \tag{2}$$

where c is the speed of light, l is the length of the resonator, and ϵ_{eff} is the effective dielectric constant calculated by

$$\epsilon_{\mathrm{eff}} = \left(1 + \epsilon_{\mathrm{sub}} \frac{K(k_1')}{K(k_1)} \frac{K(k_2)}{K(k_2')} \right) \left(1 + \frac{K(k_1')}{K(k_1)} \frac{K(k_2)}{K(k_2')} \right)^{-1}. \tag{3}$$

$K(k)$ is the complete elliptic integral of the first kind and $k_1' = \sqrt{1 - k_1^2}$ and $k_2' = \sqrt{1 - k_2^2}$. These equations allow for precise design and optimization of CPW resonators for specific applications in quantum circuits.

The frequency of ASRs can be calculated by [27, 28]

$$f_{\mathrm{ASR}} = \xi \frac{c}{\sqrt{\epsilon_{\mathrm{eff}}}} \frac{p}{2\pi (r_{\mathrm{in}} + np)^2}, \tag{4}$$

where ξ is a shape-dependent constant which is 0.81 for circular coils [27], r_{in} is the inner radius, n is the number of turns and p is the pitch which is the wire width w plus spacing. The effective dielectric constant ϵ_{eff} in this case is approximated as the average of the dielectric constants of air and substrate, $(1 + \epsilon_{\mathrm{sub}})/2$. The geometric inductance L of ARSs

can be calculated by the current-sheet method [28, 35, 36]

$$L = \frac{\mu_0 n^2 (r_{\text{out}} + r_{\text{in}}) c_1}{2} \left(\log(c_2/\rho) + c_3\rho + c_4\rho^2 \right), \tag{5}$$

where μ_0 is the vacuum permeability, r_{out} is the outer radius and ρ is the fill-ratio of the spiral given by $\rho = (r_{\text{out}} - r_{\text{in}})/(r_{\text{out}} + r_{\text{in}})$. $c_{1,2,3,4}$ are geometry dependent constants, $(1.0, 2.5, 0.0, 0.2)$ for our case [36]. Thus, the impedance can be calculated by

$$Z_{\text{ASR}} = 2\pi f_{\text{ASR}} L. \tag{6}$$

In this work, we designed CPWs and ASRs with various line widths. The fundamental resonance frequencies were designed to range from 4 GHz to 7 GHz, based on Eqs. (1) and (4). The design frequencies calculation considers only the geometric inductance and neglect kinetic inductance. This approximation is justified for our epitaxial TiN films, which are known to have a low kinetic inductance fraction [26]. The CPWs have line widths of w = 8 µm, 12 µm, and 20 µm, all with a quarter wavelength and a characteristic impedance of 50 Ω (Fig. 1(a) shows a CPW with w = 8 µm). The ASRs share similar design characteristics but vary in their line widths and gaps. They have line widths of w = 7 µm, 8 µm, 10 µm, and 12 µm, with gaps between neighboring wires matching these widths (i.e. $p = 2w$). We fixed the number of spiral turns at 12, resulting in an outer radius of $r_{\text{out}} = 12p$ and a consistent impedance of 810 Ω for all ASRs, shown in Fig. 1(b).

These resonators, including both CPWs and ASRs, are fabricated on a single 10 mm × 10 mm chip and coupled to a common feedline as shown in Fig. 1(c). To minimize parasitic slotline modes and ensure ground uniformity across the chip, on-chip airbridge bonding was implemented across the ground planes (not shown in Fig. 1(c)). This design mitigates standing wave formation and supports consistent coupling behavior. We implemented a design modification for the ASRs by extending the tail of the spiral shape to achieve capacitive coupling with the feedline. This extension decreases the fundamental frequencies of the ASRs compared to their pure spiral design, necessitating independent verification of the actual frequencies. The measured fundamental resonance frequencies of resonators with various designed width are presented in Table 1.

The measured frequencies for CPW resonators agree well with the design values, within approximately 2%, confirming the reliability of our modeling. For ASRs, the measured frequencies are consistently about 11% lower than the designed values. This systematic deviation arises primarily from the additional inductance and capacitance contributed by the resonator extensions, which are not fully captured in Eq. (4). Importantly, this downward shift is reproducible across all ASRs studied, and can thus be taken into account to target desired frequency bands. This makes the simplified model a useful and efficient tool for initial layout despite its limitations.

The devices are fabricated on a (200)-oriented 100 nm TiN film domain-matched epitaxially grown on a high-resistivity (20 kΩ · cm) silicon (100) substrate [37]. Fabrication was carried out via using photolithography followed by a hydrofluoric acid treatment to remove surface oxidation. The photolithography step employed a etching mask made with photoresist AZ1500 to pattern the TiN film through dry etching in CF_4 plasma. After removing the photoresist, O_2 ashing was conducted to eliminate residual organics. To remove any oxide generated during ashing and restore a clean surface, a time-controlled

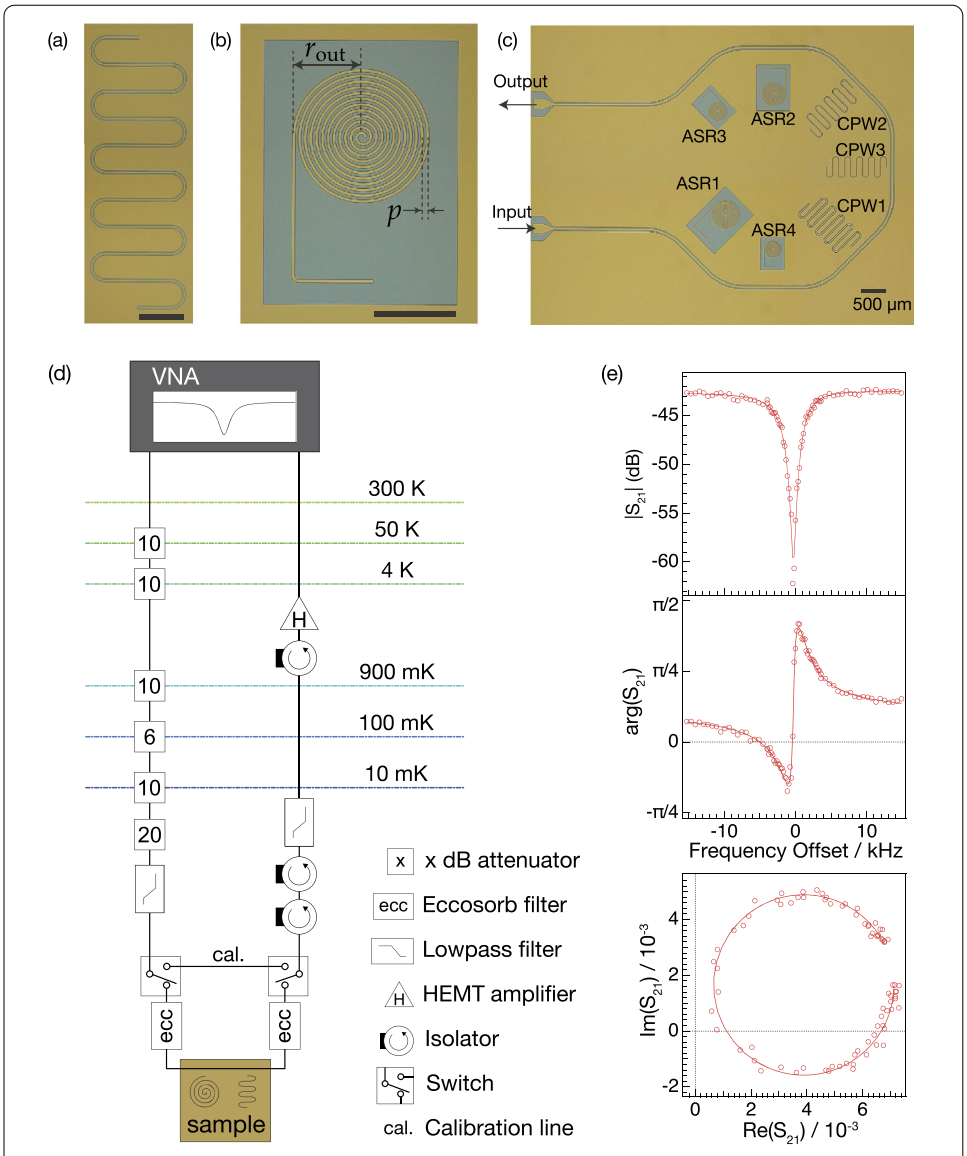

Figure 1 Experimental setup of the device. An optical microscope image of (a) a coplanar waveguide (CPW) quarter-wavelength resonator, and (b) an Archimedean Spiral Resonator (ASR) with the outer radius r_{out} and the pitch p. The scale bars in (a) and (b) indicate 200 µm, corresponding to CPW3 and ASR4 shown in (c). (c) An optical image of the chip on which the resonators are coupled to the feedline. (d) Schematic of the measurement setup. The sample is bonded to a printed circuit board in a copper sample box and cooled to 10 mK in a dilution refrigerator. The incoming signal from the vector network analyzer (VNA) is attenuated by 75.8–79.0 dB (varying with frequency) to account for attenuators, cable losses, and bonding reflection. It then passes through an 8 GHz lowpass filter and an eccosorb filter. The output signal passes through another eccosorb filter, isolators, and a lowpass filter before low-temperature amplification with a high-electron-mobility transistor (HEMT). Switches allow the signal to be routed either through the sample or directly through a calibration line for reference measurements. (e) A typical measured S_{21} parameter of the resonator is shown here for ASR3 with an average photon number of 17.6 inside the resonator. The magnitude (top) and phase (middle) are mapped to the resonance circle (bottom), with the diameter $Q_l/|Q_c|$

hydrofluoric acid treatment removed the native oxide layer. This step removes the native SiO_2 and yields a hydrogen-terminated silicon surface, with minimal exposure to ambient conditions before TiN growth, thereby limiting the formation of surface OH groups. TiN itself is chemically stable under HF treatment, and its high crystallinity helps to suppress

Table 1 Resonator specification: designed width (w), designed frequency (f_{design}) calculated from Eq. (1) and Eq. (4), measured resonance frequency (f_{meas}), and coupling quality factor (Q_{c})

Label	w/μm	f_{design}/GHz	f_{meas}/GHz	$Q_{\mathrm{c}}/10^6$
CPW1	20	4.43	4.49	1.2
CPW2	12	5.38	5.34	1.4
CPW3	8	6.28	6.17	1.7
ASR1	12	4.49	4.02	1.8
ASR2	10	5.38	4.81	1.0
ASR3	8	6.72	6.00	1.7
ASR4	7	7.69	6.85	1.6

intrinsic TLS contributions. This process ensures clean interfaces and minimizes potential loss sources in the final resonator structures.

3 Measurements and characterization

We conducted measurements of the fabricated resonators using a dilution refrigerator at a base temperature of 10 mK. The sample was bonded to a three-layer printed circuit board fabricated by Kansai Denki Industry Co., Ltd. It was mounted in a copper sample box with an aluminum lid, creating a space of 12.3 mm × 12.3 mm × 1.5 mm, with a back-drill of radius 4.3 mm and depth of 3.1 mm. A schematic of the sample package is shown in Fig. S1 (Supplemental Materials), where the cavity dimensions and back-drill geometry are illustrated. The enclosure was designed with minimized seams to suppress potential radiation loss, while the compact space and back-drill effectively raised the cut-off frequency of environmental modes.

Figure 1(d) illustrates the experimental setup. We utilized a series of attenuators 66 dB in total to reduce the incoming signal power. Taking into account cable losses and bonding reflections, the overall attenuation ranged from 75.8 to 79.0 dB, depending on the frequency (for a detailed breakdown, see Sect. 2 of Supplemental Materials). The signal then passed through an 8 GHz lowpass filter and an eccosorb filter before reaching the sample. The resonators were probed using a vector network analyzer (VNA) to measure their transmission characteristics (S_{21} parameters) over a range of input powers with a consistent resolution bandwidth of 10 Hz. The VNA output power varied from −80 dBm to 14 dBm, with an additional 16 dB attenuator placed at room temperature. Quality factors were extracted from the measured resonance curves using a circle fitting procedure [38] that accounts for both intrinsic quality factor Q_{i} and coupling quality factor Q_{c}. This method accounts for cable delay, impedance mismatch, and background transmission level, and is robust against asymmetric resonance line shapes (see Eq. (S2)).

Figure 1(e) shows a typical measured S_{21} parameter of the ASR with w = 8 μm (ASR3), mapped to the resonance circle with the diameter $Q_{\mathrm{l}}/|Q_{\mathrm{c}}|$, where Q_{l} is the load quality factor, and additional examples of measured S_{21} are provided in Fig. S3 in Supplemental Materials. We designed the Q_{c} values to be approximately equal across resonators using COMSOL simulations of the coupling structures, which provided order-of-magnitude guidance. The actual results of Q_{c} from our measurements, shown in Table 1.

Extracted Q_{i} values for ASRs and CPWs are plotted in Fig. 2. Each data point represents the harmonic mean of ten individual measurements. At low powers, the extracted Q_{i} exhibit larger uncertainties, which originate from TLS-induced fluctuations that vary between measurement sweeps even on the same device. These fluctuations can occasionally result in anomalously high Q_{i} with large fitting errors, contributing to the broad error

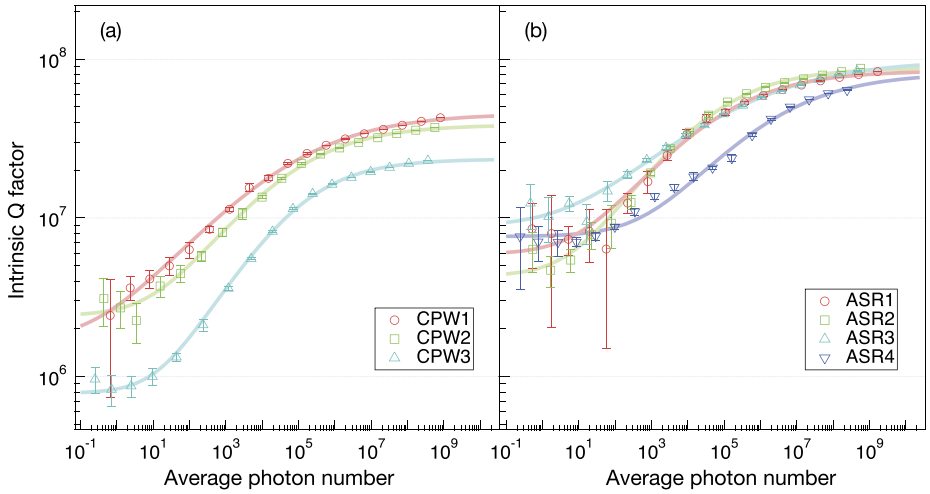

Figure 2 Extracted intrinsic quality factors of (a) CPWs and (b) ASRs. Markers are the measured quality factors, and lines are TLS fits using Eq. (7)

Table 2 Measured and calculated parameters characterizing resonator performance. The loss tangent multiplied by surface participation ($p\,\delta_{\mathrm{TLS}}$), single-photon quality factor ($Q_{\mathrm{i,0}}$), and high-power quality factor ($Q_{\mathrm{i,high}}$) are obtained through transmission (S_{21}) measurements and TLS fits, with results shown in Fig. 2. The participation ratios of metal-air (MA), metal-substrate (MS), and substrate-air (SA) interfaces—p_{MA}, p_{MS}, and p_{SA}, respectively—are calculated using the finite element solver COMSOL. The total surface participation (p_{tot}) is the sum of p_{MA}, p_{MS}, and p_{SA}

Label	$p\,\delta_{\mathrm{TLS}}/10^{-8}$	$Q_{\mathrm{i,0}}/10^5$	$Q_{\mathrm{i,high}}/10^6$	$p_{\mathrm{MA}}/10^{-5}$	$p_{\mathrm{MS}}/10^{-5}$	$p_{\mathrm{SA}}/10^{-5}$	$p_{\mathrm{tot}}/10^{-5}$
CPW1	58 ± 31	17.3 ± 9.3	45.50 ± 0.88	5.60	56.50	54.81	116.91
CPW2	38.8 ± 5.7	25.8 ± 3.8	38.59 ± 0.59	9.41	88.42	87.90	185.73
CPW3	123 ± 28	8.13 ± 1.9	23.46 ± 0.32	14.50	128.03	129.52	272.05
ASR1	15.8 ± 4.5	63 ± 18	84.5 ± 2.3	2.66	30.84	25.19	58.69
ASR2	22.1 ± 6.2	45 ± 13	88.0 ± 1.5	3.06	34.31	28.82	66.19
ASR3	10.4 ± 1.6	96 ± 15	99.1 ± 3.9	3.67	39.68	34.40	77.75
ASR4	11.9 ± 1.3	84.0 ± 9.3	81.8 ± 6.3	4.12	43.59	38.44	86.15

bars observed in Fig. 2. The error bars represent standard 1-sigma fitting uncertainties propagated from the individual complex S_{21} circle fits.

Here, we observed a clear power dependence in the quality factors Q_{i}, with the highest Q_{i} achieved at high input powers where the effects of two-level systems are saturated. The power dependence of the Q_{i} of the resonator is described by the TLS model [39, 40]:

$$\frac{1}{Q_{\mathrm{i}}} = \tan\delta \simeq p\,\delta_{\mathrm{TLS}} \frac{\tanh\left(\frac{hf}{2kT}\right)}{\sqrt{1+\left(\frac{\langle n\rangle}{n_{\mathrm{c}}}\right)^{\beta}}} + \delta_{\mathrm{e}}, \tag{7}$$

where p is the total energy participation ratio, δ_{TLS} is the ensemble TLS loss tangent due to resonant absorption, $\langle n\rangle$ is the average photon number in resonators, n_{c} is the critical photon number at which TLS saturation occurs, and δ_{e} is the power-independent contribution to the total loss. β is an empirical parameter which describes TLS interaction. The measurement results are fit to Eq. (7), allowing us to extract $p\,\delta_{\mathrm{TLS}}$ as shown in Table 2.

Our measurements revealed that the spiral resonators consistently outperformed their CPW counterparts across all power levels. At single-photon energies, the ASRs maintained intrinsic quality factors 2–4 times higher than CPWs of comparable dimensions. Our best-performing ASR exhibited an exceptional intrinsic quality factor reaching 10 million, with $Q_{\mathrm{i},0} \equiv (p\,\delta_{\mathrm{TLS}})^{-1} = (9.6 \pm 1.5) \times 10^6$ at the single-photon level, and $Q_{\mathrm{i,high}} \equiv (\delta_{\mathrm{e}})^{-1} = (9.91 \pm 0.39) \times 10^7$ at high power. Table 2 presents the single-photon intrinsic quality factor $Q_{\mathrm{i},0}$ and high-power intrinsic quality factor $Q_{\mathrm{i,high}}$ for all resonators.

While the ASRs exhibit higher average Q_{i} than the CPWs, we acknowledge that the statistical spread caused by temporal fluctuations of TLS loss leads to some overlap in the measured Q_{i} values. Supplemental Fig. S4 shows the distribution of loss tangent obtained over a 24-hour period. Despite this overlap, the trend that ASRs yield higher values on average remains robust.

We note that radiation loss is a well-known issue for resonators due to their open geometry. In our devices, ASR resonators are expected to be more sensitive to radiation loss compared to CPW resonators due to their more open structures that could enhance coupling to free-space modes. Nevertheless, the ASRs consistently exhibited higher Q_{i} than the CPWs on the same chip. This observation suggests that radiation loss is not the dominant limitation for either type of resonator in our experiments. It indicates that our packaging design effectively suppresses radiation loss, allowing intrinsic TLS-related losses to dominate the performance.

4 Surface participation ratio

To elucidate the superior performance of ASRs, we computed the surface participation ratios (PRs) of resonators. We categorized the key interfaces into three types: metal-air (MA), metal-substrate (MS), and substrate-air (SA). By analyzing these interfaces separately, we assessed their individual contributions to loss. The total loss tangent associated with these interfaces is given by

$$\tan\delta = \sum_i p_i \tan\delta_i, \tag{8}$$

where p_i denotes the PR of interface i = MA, MS, or SA and interface i has loss tangent δ_i. PR quantifies the fraction of the electromagnetic energy U_i stored at amorphous interfaces relative to the total energy U_{tot}:

$$p_i = \frac{U_i}{U_{\mathrm{tot}}} = \int_i dxdydz\, \frac{\epsilon_i}{2} \left|\boldsymbol{E}(x,y,z)\right|^2 / U_{\mathrm{tot}} \tag{9}$$

for the interface material with dielectric constant ϵ_i.

We conducted 2D static calculations using COMSOL. For CPWs, we adopted a calculation method similar to that described in Ref. [41], modeling them as infinitely long rectangular metal plates, as shown in Fig. 3(a). ASRs were approximated as sets of concentric rings using axially symmetric modeling, as shown in Fig. 3(b).

In addition, we introduce an approximation that the electric field $\boldsymbol{E}$ is uniform over the thin lossy layer, allowing us to calculate the PR solely from the electric field on the surface. This approximation holds for most of the structure, except for the peripheral region of the metal where field variations are more significant [30, 41]. When we take the x-axis parallel

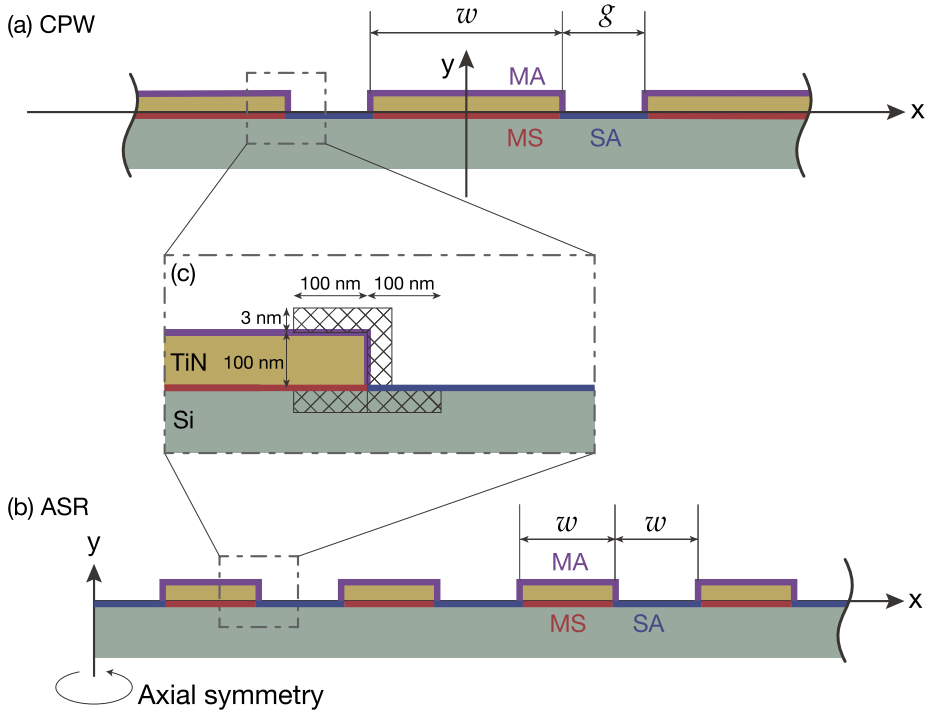

Figure 3 The schematic illustration of the model for 2D simulation of PRs shows: (a) a CPW with width *w* and gap *g*, and (b) an ASR with width *w* and spacing *w*. The ASR is approximated as a set of concentric rings using axially symmetric modeling. The three interfaces are depicted in purple (MA), red (MS), and blue (SA). (c) A detailed model of the metal edge, where a 3 nm layer within 100 nm of the peripheral region is modeled, as indicated by the cross-hatched area

to the surface of the substrate and the y-axis perpendicular to it, the continuity of electric displacement requires:

$$E_x^{\mathrm{sim},i} = E_x^i \tag{10}$$

$$\epsilon_{\mathrm{sim},i} E_y^{\mathrm{sim},i} = \epsilon_i E_y^i, \tag{11}$$

where the subscript i = MA, MS, or SA refers to the lossy interface the actual sample contains and 'sim, i' the material present in the simulation instead of the actual material of i. Here, we supposed $\epsilon_i = 10$ for all i and we used $\epsilon_{\mathrm{sim,MA}} = \epsilon_{\mathrm{air}} = 1$, $\epsilon_{\mathrm{sim,MS}} = \epsilon_{\mathrm{Si}} = 11.45$ and $\epsilon_{\mathrm{sim,SA}} = (\epsilon_{\mathrm{air}} + \epsilon_{\mathrm{Si}})/2 = 6.225$ for the relative dielectric constant. Thus, the PR in the internal region of the metal should be calculated by

$$p_i = t \int_i dxdy \, \frac{\epsilon_i}{2} \left(\left| E_x^{\mathrm{sim},i} \right|^2 + \left| \frac{\epsilon_{\mathrm{sim},i}}{\epsilon_i} E_y^{\mathrm{sim},i}(x) \right|^2 \right) / U_{\mathrm{tot}}, \tag{12}$$

where t represents the thickness of the hypothetical lossy layer. Here we supposed $t = 3$ nm, which is consistent with prior modeling practices in the literature [30, 31]. This thickness is not experimentally measured in our study and is used only for order-of-magnitude estimates. While fabrication steps such as CF_4 etching and subsequent HF cleaning are expected to influence the surface composition, the comparative nature of our analysis (both

CPWs and ASRs fabricated on the same die) makes the relative trends in PR robust against such uncertainties in absolute thickness.

Using the continuity conditions of electric displacement, we can calculate the electric field in the thin layer without explicitly modeling it in internal regions, significantly reducing computational costs. However, the peripheral region still requires detailed modeling due to its more complex field distribution. We modeled the 3 nm layer within 100 nm of the peripheral region as shown in Fig. 3(c) and calculated PRs using Eq. (9).

The voltage distribution $V(x)$ in an ASR can be expressed as a function of the radial distance x from the center:

$$V(x) = V_0 \cos\left(\pi \left(\frac{x}{r_{\text{out}}}\right)^2\right) \tag{13}$$

where V_0 is the applied voltage and r_{out} is the outer radius of the spiral. This analytical solution allows for efficient calculation of the electric field distribution, which is crucial for accurate PR calculations. The validity of Eq. (13) was checked using COMSOL simulation (see Sect. 5 of Supplemental Materials).

Our COMSOL simulations revealed that ASRs have significantly lower PRs compared to CPWs, as presented in Table 2. The total surface participation (p_{tot}) is the sum of p_{MA}, p_{MS}, and p_{SA}. This reduction in PR largely explains the superior Q_{i} values of ASRs, even when considering coarse approximations such as modeling a spiral with rings.

Figure 4 shows the relationship between the experimentally extracted and calculated loss tangent on a log-log scale. Because the error distribution of the loss tangent follows a log-normal distribution (see Sect. 4 of Supplemental Materials), a log-log representation provides a more appropriate visualization. At low power levels, the loss tangent fluctuates due to variations in the TLS state, as shown in Fig. S4, occasionally leading to large experimental values. The dataset was obtained in a single continuous measurement sequence.

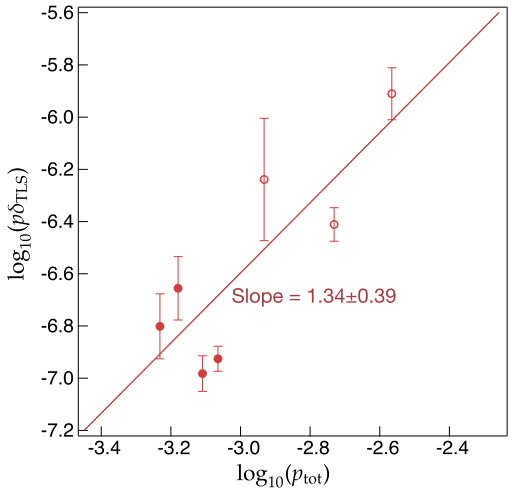

Figure 4 The relationship between experimentally extracted loss tangent values $p\,\delta_{\text{TLS}}$ and calculated total participation ratios p_{tot}. The vertical axis represents $\log(p\tan\delta)$ while the horizontal axis represents $\log(p_{\text{tot}})$. Filled circles correspond to ASR data, while open circles represent CPW data. A linear fit to the data yields a slope of 1.34 ± 0.39. The error bars represent fitting errors obtained from Fig. 2, propagated through logarithmic transformation

While individual data points may deviate from a linear trend due to the temporal fluctuations in the TLS configuration, the overall linear fit remains a valid approach for assessing the underlying correlation between simulated and measured loss. A linear fit to the data yields a slope of 1.34 ± 0.39, which, given the uncertainty, is consistent with the ideal value of unity. This agreement confirms the validity of the PR simulation, as a slope near unity indicates that the model accurately captures the dominant loss mechanisms. The slight deviation from unity suggests that additional loss sources, such as bulk loss [42] or other surface-related effects [43], may also contribute, though they do not dominate the behavior.

The decreased surface participation directly correlates with the observed reduction in TLS induced losses, resulting in enhanced resonator performance. The MS and SA interfaces still contribute significantly to loss. Future designs that reduce the PR at these interfaces could lead to substantial improvements in resonator performance.

5 Conclusion

In conclusion, our study demonstrates the potential of spiral geometry in superconducting resonators for achieving high intrinsic quality factors. Using domain-matched epitaxially grown titanium nitride on silicon wafers, we have fabricated Archimedean spiral resonators with high quality factors, achieving $Q_i = (9.6 \pm 1.5) \times 10^6$ at the single-photon level and $Q_i = (9.91 \pm 0.39) \times 10^7$ at high power. Our numerical analysis revealed that the superior performance of our spiral resonators compared to traditional coplanar waveguide resonators is explained by their lower participation ratios at lossy interfaces, which result from a more evenly distributed electromagnetic field. These results suggest that spiral resonators could be a promising alternative to traditional coplanar waveguide designs, particularly in applications requiring minimal coupling to two-level systems, such as quantum computing and quantum sensing. Furthermore, the high-Q_i performance of our spiral resonators may provide a platform for studying the dynamics of two-level systems.

While these results are promising, the metal-substrate and substrate-air interfaces still contribute significantly to losses. Future work could explore further optimizations of the spiral geometry, such as varying the width along the spiral or incorporating other design elements to reduce surface participation further. Additionally, investigating the performance of these spiral resonators in different material systems such as niobium, aluminum, or tantalum could provide deeper insights into the material-dependent losses [33, 44]. Exploring alternative wafer materials, such as sapphire [45] or silicon-on-insulator [46], could also provide insights into the role of substrate-induced losses and help identify the fundamental limits of superconducting resonators for further improvement.

These improvements address the challenge of enhancing the scalability and reliability of superconducting quantum circuits, including the implementation of bosonic code quantum error correction, and may also contribute to advances in quantum sensing, such as dark matter searches with qubits [47].

While the results presented here are based on measurements from a single die containing both ASR and CPW resonators, systematic studies across multiple dies and fabrication runs were not performed in this work. Evaluating the reproducibility and uniformity of the Q factors across different chips and fabrication batches remains an important direction for future investigation.

Supplementary information

Supplementary information accompanies this paper at https://doi.org/10.1140/epjqt/s40507-025-00367-w.

Additional file 1. (PDF 9.4 MB)

Acknowledgements
The authors acknowledge the Superconducting Quantum Electronics Research Team, the Superconducting Quantum Computing System Research Unit, and the Semiconductor Science Research Support Team for their support in device fabrication at the RIKEN Nanoscience Joint Laboratory. We also thank G. Ando, Y. Matsuyama, and Y. Tsuchimoto for their assistance in experiments, and S. Tamate for valuable insights into the PR calculation methods.

Author contributions
This project was conceptualized and led by A.N., S.S., and Y.T. Y.H, and H.T prepared domain-matched epitaxially grown TiN films. Y.T. carried out sample design, fabrication, measurements, and data analysis, with support from S.S. Y.T. drafted the manuscript, which was reviewed and approved by all authors.

Funding information
This research has been supported by funding from JST Moonshot R&D Program (Grant Number JPMJMS2067), JST ERATO (Grant Number JPMJER2302), JST CREST (Grant Number JPMJCR24I5), MEXT Q-LEAP (Grant Number JPMXS0118068682), and JSPS KAKENHI (Grant Numbers JP24H00832 and JP24K22871).

Data availability
No datasets were generated or analysed during the current study.

Materials availability
Not applicable.

Code availability
Not applicable.

Declarations

Ethics approval and consent to participate
Not applicable.

Consent for publication
Not applicable

Competing interests
The authors declare no competing interests.

Author details
[1]RIKEN Center for Quantum Computing, Wako, 351-0198 Saitama, Japan. [2]Komaba Institute for Science (KIS), The University of Tokyo, Meguro-ku, 153-8902, Tokyo, Japan. [3]Advanced ICT Research Institute, National Institute of Information and Communications Technology (NICT), Kobe, 651-2492 Hyogo, Japan. [4]Inamori Research Institute for Science (InaRIS), Kyoto-shi, 600-8411 Kyoto, Japan.

Received: 27 February 2025 Accepted: 16 May 2025 Published online: 13 June 2025

References

1. Blais A, Huang R-S, Wallraff A, Girvin SM, Schoelkopf RJ. Cavity quantum electrodynamics for superconducting electrical circuits: an architecture for quantum computation. Phys Rev A, At Mol Opt Phys. 2004;69:062320.
2. Wallraff A, et al. Strong coupling of a single photon to a superconducting qubit using circuit quantum electrodynamics. Nature. 2004;431:162–7.
3. Sillanpää MA, Park JI, Simmonds RW. Coherent quantum state storage and transfer between two phase qubits via a resonant cavity. Nature. 2007;449:438–42.
4. Bergeal N, et al. Phase-preserving amplification near the quantum limit with a Josephson ring modulator. Nature. 2010;465:64–8.
5. Day PK, LeDuc HG, Mazin BA, Vayonakis A, Zmuidzinas J. A broadband superconducting detector suitable for use in large arrays. Nature. 2003;425:817–21.
6. Hofheinz M, et al. Synthesizing arbitrary quantum states in a superconducting resonator. Nature. 2009;459:546–9.
7. Joshi A, Noh K, Gao YY. Quantum information processing with bosonic qubits in circuit qed. Quantum Sci Technol. 2021;6:033001.
8. Terhal BM, Conrad J, Vuillot C. Towards scalable bosonic quantum error correction. Quantum Sci Technol. 2020;5:043001.
9. Kudra M, et al. High quality three-dimensional aluminum microwave cavities. Appl Phys Lett. 2020;117.
10. Heidler P, et al. Non-Markovian effects of two-level systems in a niobium coaxial resonator with a single-photon lifetime of 10 milliseconds. Phys Rev Appl. 2021;16:034024.
11. Milul O, et al. Superconducting cavity qubit with tens of milliseconds single-photon coherence time. PRX Quantum. 2023;4:030336.

12. Sivak V, et al. Real-time quantum error correction beyond break-even. Nature. 2023;616:50–5.
13. Ni Z, et al. Beating the break-even point with a discrete-variable-encoded logical qubit. Nature. 2023;616:56–60.
14. Goetz J, et al. Loss mechanisms in superconducting thin film microwave resonators. J Appl Phys. 2016;119.
15. Vissers MR, et al. Low loss superconducting titanium nitride coplanar waveguide resonators. Appl Phys Lett. 2010;97.
16. Quintana C, et al. Characterization and reduction of microfabrication-induced decoherence in superconducting quantum circuits. Appl Phys Lett. 2014;105.
17. Sage JM, Bolkhovsky V, Oliver WD, Turek B, Welander PB. Study of loss in superconducting coplanar waveguide resonators. J Appl Phys. 2011;109.
18. Megrant A, et al. Planar superconducting resonators with internal quality factors above one million. Appl Phys Lett. 2012;100.
19. Richardson CJ, et al. Fabrication artifacts and parallel loss channels in metamorphic epitaxial aluminum superconducting resonators. Supercond Sci Technol. 2016;29:064003.
20. Shi L, et al. Tantalum microwave resonators with ultra-high intrinsic quality factors. Appl Phys Lett. 2022;121.
21. Lei CU, Krayzman L, Ganjam S, Frunzio L, Schoelkopf RJ. High coherence superconducting microwave cavities with indium bump bonding. Appl Phys Lett. 2020;116.
22. Ganjam S, et al. Surpassing millisecond coherence in on chip superconducting quantum memories by optimizing materials and circuit design. Nat Commun. 2024;15:3687.
23. Shalibo Y, et al. Lifetime and coherence of two-level defects in a Josephson junction. Phys Rev Lett. 2010;105:177001.
24. Martinis JM, et al. Decoherence in Josephson qubits from dielectric loss. Phys Rev Lett. 2005;95:210503.
25. Phillips WA. Tunneling states in amorphous solids. J Low Temp Phys. 1972;7:351–60.
26. Vissers MR, Weides MP, Kline JS, Sandberg M, Pappas DP. Identifying capacitive and inductive loss in lumped element superconducting hybrid titanium nitride/aluminum resonators. Appl Phys Lett. 2012;101.
27. Maleeva N, et al. Electrodynamics of planar Archimedean spiral resonator. J Appl Phys. 2015;118.
28. Peruzzo M, Trioni A, Hassani F, Zemlicka M, Fink JM. Surpassing the resistance quantum with a geometric superinductor. Phys Rev Appl. 2020;14:044055.
29. COMSOL 6.0 (www.comsol.com).
30. Wang C, et al. Surface participation and dielectric loss in superconducting qubits. Appl Phys Lett. 2015;107.
31. Calusine G, et al. Analysis and mitigation of interface losses in trenched superconducting coplanar waveguide resonators. Appl Phys Lett. 2018;112.
32. Woods W, et al. Determining interface dielectric losses in superconducting coplanar-waveguide resonators. Phys Rev Appl. 2019;12:014012.
33. Melville A, et al. Comparison of dielectric loss in titanium nitride and aluminum superconducting resonators. Appl Phys Lett. 2020;117.
34. Ghione G, Naldi CU. Coplanar waveguides for mmic applications: effect of upper shielding, conductor backing, finite-extent ground planes, and line-to-line coupling. IEEE Trans Microw Theory Tech. 1987;35:260–7.
35. Medahinne M, et al. Magnetic field tolerant superconducting spiral resonators for circuit qed. 2024. arXiv preprint. arXiv:2406.10386.
36. Mohan SS, del Mar Hershenson M, Boyd SP, Lee TH. Simple accurate expressions for planar spiral inductances. IEEE J Solid-State Circuits. 1999;34:1419–24.
37. Sun R, Makise K, Qiu W, Terai H, Wang Z. Fabrication of (200)-oriented tin films on si (100) substrates by dc magnetron sputtering. IEEE Trans Appl Supercond. 2014;25:1–4.
38. Probst S, Song F, Bushev PA, Ustinov AV, Weides M. Efficient and robust analysis of complex scattering data under noise in microwave resonators. Rev Sci Instrum. 2015;86.
39. Phillips WA. Two-level states in glasses. Rep Prog Phys. 1987;50:1657.
40. Wang H, et al. Improving the coherence time of superconducting coplanar resonators. Appl Phys Lett. 2009;95.
41. Wenner J, et al. Surface loss simulations of superconducting coplanar waveguide resonators. Appl Phys Lett. 2011;99.
42. Zhang Z-H, et al. Acceptor-induced bulk dielectric loss in superconducting circuits on silicon. 2024. arXiv preprint. arXiv:2402.17155.
43. De Graaf S, et al. Two-level systems in superconducting quantum devices due to trapped quasiparticles. Sci Adv. 2020;6:eabc5055.
44. Wang C, et al. Towards practical quantum computers: transmon qubit with a lifetime approaching 0.5 milliseconds. npj Quantum Inf. 2022;8:3.
45. Deng H, et al. Titanium nitride film on sapphire substrate with low dielectric loss for superconducting qubits. Phys Rev Appl. 2023;19:024013.
46. Keller AJ, et al. Al transmon qubits on silicon-on-insulator for quantum device integration. Appl Phys Lett. 2017;111.
47. Dixit AV, et al. Searching for dark matter with a superconducting qubit. Phys Rev Lett. 2021;126:141302.

Publisher's note